

ISOTROPIC AGN HEATING WITH SMALL RADIO QUIET BUBBLES IN THE NGC 5044 GROUP

LAURENCE P. DAVID¹, CHRISTINE JONES^a, SIMONA GIACINTUCCI^a, WILLIAM FORMAN^a, PAUL NULSEN^a,
JAN VRTILEK^a, EWAN O'SULLIVAN^a AND SOME RAYCHAUDHURY²¹ HARVARD-SMITHSONIAN CENTER FOR ASTROPHYSICS, 60 GARDEN ST., CAMBRIDGE, MA 02138² SCHOOL OF PHYSICS AND ASTRONOMY, UNIVERSITY OF BIRMINGHAM, BIRMINGHAM B15 2TT*submitted to The Astrophysical Journal*

ABSTRACT

A Chandra observation of the X-ray bright group NGC 5044 shows that the X-ray emitting gas has been strongly perturbed by recent outbursts from the central AGN and also by motion of the central dominant galaxy relative to the group gas. The NGC 5044 group hosts many small radio quiet cavities with a nearly isotropic distribution, cool filaments, a semi-circular cold front and a two-armed spiral shaped feature of cool gas. A GMRT observation of NGC 5044 at 610 MHz shows the presence of extended radio emission with a "torus-shaped" morphology. The largest X-ray filament appears to thread the radio torus, suggesting that the lower entropy gas within the filament is material being uplifted from the center of the group. The radio emission at 235 MHz is much more extended than the emission at 610 MHz, with little overlap between the two frequencies. One component of the 235 MHz emission passes through the largest X-ray cavity and is then deflected just behind the cold front. A second detached radio lobe is also detected at 235 MHz beyond the cold front. All of the smaller X-ray cavities in the center of NGC 5044 are undetected in the GMRT observations. Since the smaller bubbles are probably no longer momentum driven by the central AGN, their motion will be affected by the group "weather" as they buoyantly rise outward. Hence, most of the enthalpy within the smaller bubbles will likely be deposited near the group center and isotropized by the group weather. The total mechanical power of the smaller radio quiet cavities is $P_c = 9.2 \times 10^{41} \text{erg s}^{-1}$ which is sufficient to suppress about one-half of the total radiative cooling within the central 10 kpc. This is consistent with the presence of H α emission within this region which shows that at least some of the gas is able to cool. The mechanical heating power of the larger southern cavity, located between 10 and 20 kpc, is six times greater than the combined mechanical power of the smaller radio quiet cavities and could suppress all radiative cooling within the central 25 kpc if the energy were deposited and isotropized within this region. Within the central 20 kpc, emission from LMXBs is a significant component of the X-ray emission above 2 keV. The presence of hard X-ray emission from unresolved LMXBs makes it difficult to place strong constraints on the amount of shock heated gas within the X-ray cavities.

Subject headings: galaxies:clusters:general – cooling flows – intergalactic medium – galaxies:active – X-rays:galaxies:clusters

1. INTRODUCTION

Chandra and XMM-Newton observations of groups and clusters of galaxies have led to significant changes in the cooling flow model (e.g., McNamara et al. 2000; David et al. 2001; Fabian et al. 2003; Blanton et al. 2003; Peterson et al. 2003; Nulsen et al. 2005; Peterson & Fabian 2006; Forman et al. 2007; McNamara & Nulsen 2007 and references therein). The primary revision to the cooling flow model has been the addition of a strong feedback mechanism between the central AGN and the cooling of the hot gas. AGN outbursts in the central dominant galaxy in groups and clusters, which are themselves fueled by the accretion of cooling gas, can produce shocks, cavities and sound waves, all of which lead to re-heating of the cooling gas. This AGN-cooling flow feedback mechanism is also an important process in galaxy formation and can help explain the observed correlation between bulge mass (or stellar velocity dispersion) and central black hole mass (e.g., Gebhardt et al. 2000) and the cut-off in the number of massive galaxies (Croton et al. 2006). There have been extensive studies with deep Chandra and XMM-Newton observations of several rich clusters (e.g., Perseus - Fabian et al. 2006; Centaurus - Fabian et al. 2005; Virgo - Forman et al. 2007) that show the full complexity of AGN induced structure in the hot gas, but far fewer detailed studies of the the AGN-cooling flow connection in groups of galaxies, which harbor the majority of baryonic matter in the universe. In addition to AGN induced X-ray features in groups and clusters, motion of the central dominant

galaxy relative to the hot gas can also produce sharp fronts in the X-ray images (see Markevitch & Vikhlinin 2007 for a review). In this paper, we present the results of a moderately deep Chandra observation of the X-ray bright NGC 5044 group of galaxies and discuss the variety of AGN and motion induced features evident in the X-ray data.

The NGC 5044 group of galaxies is one of the X-ray brightest groups in the sky with a redshift of $z=0.009$. The large scale X-ray morphology of the NGC 5044 group, as revealed by a ROSAT PSPC observation, is very smooth and nearly spherically symmetric (David et al. 1995). Within the central 20 kpc, however, there were some indications from the PSPC observation that the group is not fully relaxed. The PSPC image showed that the peak of the X-ray emission in the group, which is coincident with the optical centroid of NGC 5044, is off-set from the centroid of the outer X-ray contours, suggesting that NGC 5044 is in motion with respect to the center of the group potential. A "tear drop" shaped feature of cooler gas extending to the south-east from NGC 5044 was also detected in the PSPC image. This was interpreted as a cooling wake by David et al. (1995), i.e., cooling gas that was gravitationally focused into the wake of NGC 5044. ASCA observations of NGC 5044 also showed evidence for multi-phase gas in the center of the group (Buote 1999).

NGC 5044 was previously observed by Chandra for 20 ksec on Mar. 19, 2000. A joint analysis of this earlier Chandra observation and a XMM-Newton observation by Buote et al. (2003)

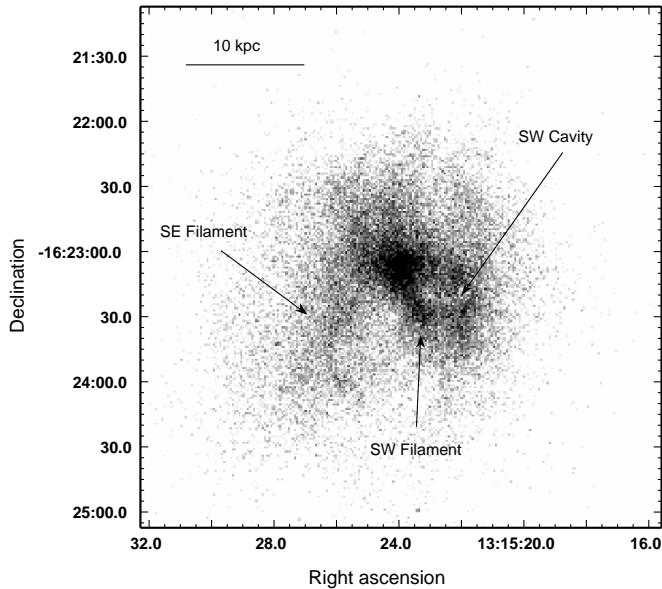


FIG. 1.— Raw 0.3-2.0 keV ACIS image of the central 4' by 4' (44 kpc by 44 kpc) region of NGC 5044.

found evidence for multiphase gas within the central 30 kpc. Gastaldello et al. (2008) noted the presence of two cavities, several cool filaments and a cold front approximately 30 kpc toward the south-east from NGC 5044 in the earlier ACIS observation. The XMM-Newton observation of NGC 5044 showed that there is an additional cold front approximately 50 kpc toward the north-west from NGC 5044 (Buote et al. 2003). Analysis of the XMM-Newton RGS data for NGC 5044 by Tamura et al. (2003) found that the emission from within the central 20 kpc is well represented by a two temperature model with $kT=0.7$ and 1.1 keV. This range in temperatures is consistent with the gas temperatures seen in projection based on the temperature profiles previously derived from ROSAT (David et al. 1995) and XMM-Newton EPIC (Buote et al. 2003) data.

This paper is organized in the following manner. Details of the ACIS data analysis are described in §2. The complex X-ray morphology in the ACIS image is discussed in §3. In §4, we present temperature, pressure and entropy maps of the central region of NGC 5044. X-ray surface brightness profiles are presented in §5 and gas temperature profiles are presented in §6. Section 7 discusses the spectral analysis of the X-ray cavities and filaments. In §8 we discuss the main implications of our results concerning the AGN-cooling flow feedback mechanism and the possibility of sloshing induced cold fronts in the center of the group. A summary of our main results is given in §9. Throughout this paper we use a luminosity distance of $D_L = 38.8$ Mpc for NGC 5044, which corresponds to $1'' = 185$ pc.

2. CHANDRA DATA ANALYSIS

The NGC 5044 group of galaxies was observed by the Chandra X-ray Observatory on March 3, 2008 for a total of 82710 sec (OBSID 9399). The center of the group was positioned on the center of the back-side illuminated ACIS-S3 chip. All data analysis was performed with CIAO 4.0.1 and CALDB 3.4.3. This analysis includes the latest cti-corrected calibration products and time dependent gain corrections for the 5 chips (S1,S2,S3,I2 and I3) that were turned on during the observation. Since the X-ray emission from NGC 5044 completely fills the S3 chip, the back-side illuminated chip S1 was used to

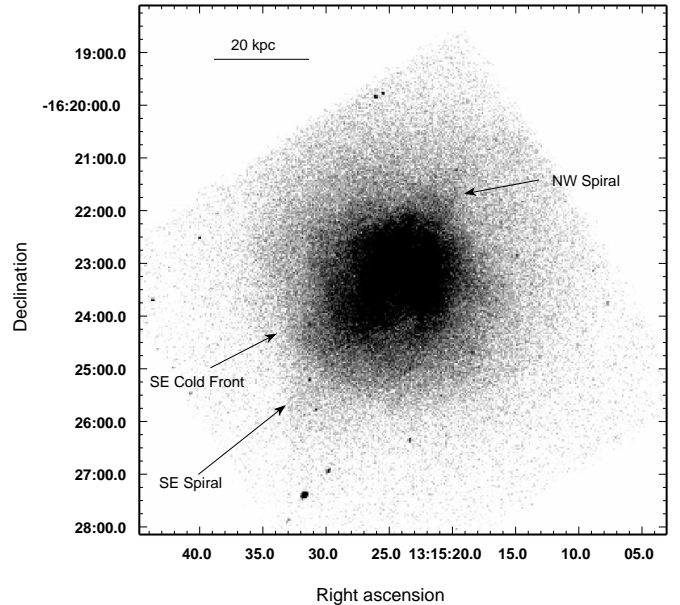


FIG. 2.— Raw 0.3-2.0 keV ACIS-S3 image of the central 10' by 10' (110 kpc by 110 kpc) region of NGC 5044.

screen for background flares. Light curves were made in the 2.5-7.0 keV and 9.0-12.0 keV energy bands for the diffuse emission on S1. No background flares exceeding a count rate threshold of 20% above the quiescent background count rate were detected during the observation. NGC 5044 was observed near solar minimum, during which time background flares were significantly reduced. Background images for the 5 chips that were turned on during the observation were extracted from the standard set of cti-corrected ACIS blank sky images in the Chandra CALDB. The exposure time in each background image was adjusted to produce the same 9.0-12.0 keV count rate as that in the NGC 5044 observation. The 9.0-12.0 keV count rates in the NGC 5044 observation were approximately 30% higher than the rates in the standard background images, which is consistent with the increasing background rate during the few years leading up to solar minimum (Markevitch 2008). The NGC 5044 observation was carried-out in very faint (VF) telemetry format and the VF background filtering was applied using the CIAO tool *acis_process_events*. The same VF background screening was applied to the background data sets by only including events with "status=0".

3. THE PERTURBED INNER REGION OF NGC 5044

3.1. Cavities, Filaments and Fronts

The ACIS images in Figs. 1 and 2 show that the central region of NGC 5044 is highly perturbed with many cavities, filaments and edges. Most of the cavities in NGC 5044 are fairly small, with diameters of only a few kpc, compared to the cavities found in rich clusters, which typically have diameters of tens of kpc (McNamara & Nulsen 2007). Also, the inner cavities in NGC 5044 have a more isotropic distribution about the center of the group compared to the nearly bipolar distribution of the larger, more energetic, cavities seen in richer systems. The central X-ray morphology of NGC 5044 is more similar to that of M87, which has many small cavities and filaments (Forman et al. 2007). The largest filament identified in Fig. 1 extends approximately 20 kpc toward the south-east.

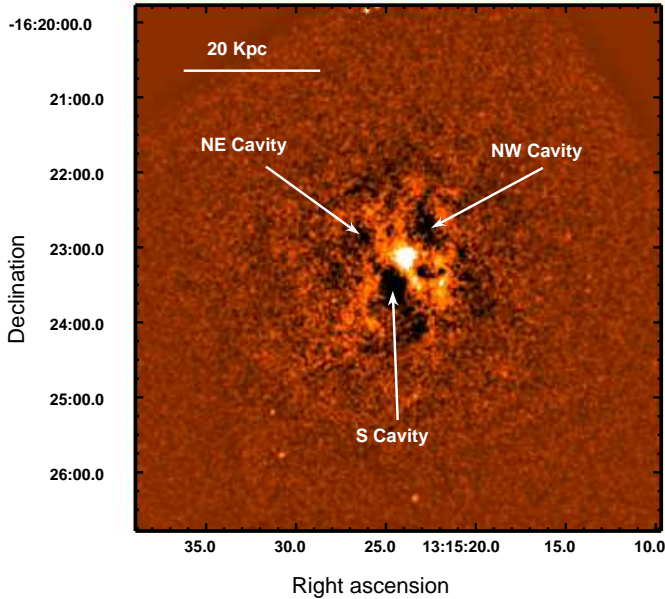


FIG. 3.— ACIS-S3 unsharp masked image of NGC 5044 in the 0.3-2.0 keV band.

Beyond the central cavities and filaments, there are two edges toward the south-east and one toward the north-west (see Fig. 2). The spectral analysis presented below (see §6) shows that all of these edges are cold fronts and not shocks (i.e., the gas interior to the fronts is cooler than the surrounding gas). The innermost cold front located 30 kpc toward the south-east was noted by Gastaldello et al. (2008) based on the earlier Chandra observation. Another cold front is also visible toward the south-east in Fig 2 with more of a spiral pattern and extends approximately 50 kpc toward the south. A corresponding spiral shaped cold front is also seen in Fig. 2 toward the north-west. This spiral feature is more obvious in the surface brightness analysis presented below. Cold fronts are commonly found near the central dominant galaxy in clusters and may be due to merger induced sloshing of the central galaxy (Markevitch & Vikhlinin 2007; Ascasibar & Markevitch 2006). However, the two-arm spiral pattern in NGC 5044 is more similar to the AGN inflated "hour glass" shape feature observed in NGC 4636 (Jones et al. 2002; O'Sullivan, Vrtilik & Kempner 2005; Baldi et al. 2009). The origin of the cold fronts in NGC 5044 will be discussed in more detail below. The full complexity of the X-ray morphology of NGC 5044 is best revealed in the unsharp masked image shown in Fig. 3. This image shows the full extent of the X-ray cavities and the enhancements in the surface brightness around the cavities. There are also several larger and weaker depressions in the unsharp masked image beyond the cavities identified in Fig. 3. It is obvious from Fig. 3 that the cavities occupy a significant fraction of the total volume within the central 10 kpc.

3.2. Radio Morphology

NGC 5044 was recently observed by the Giant Metrewave Radio Telescope (GMRT) at frequencies of 235, 325 and 610 MHz as part of a sample of groups (Giacintucci et al. 2009a). Previous higher frequency observations of NGC 5044 only detected a compact radio source with a flat spectral index consistent with a core-dominated source (Sparks et al. 1984). The GMRT observation at 610 MHz shows the presence of extended emission toward the south-east with a total flux of 8.5 mJy (see Fig. 4).

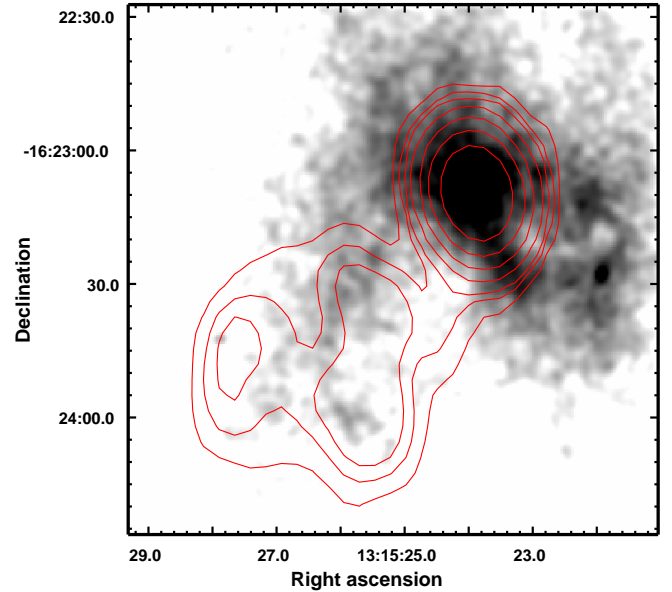


FIG. 4.— GMRT 610 MHz contours overlaid on the raw 0.3-2.0 keV ACIS image. The beam size is $18''$ by $13''$ and the lowest radio contour is shown at $3\sigma = 0.2\text{mJy/b}$.

The two off-set peaks in the 610 MHz radio image visible in Fig. 4 suggest that the 610 MHz radio emission arises from within a torus shaped region with the axis of the torus in the plane of the sky. This figure also shows that the cool gas in the SE filament appears to be threading the center of the torus. This behavior is very similar to that seen in numerical simulations of buoyantly rising AGN inflated bubbles which develop into torus-like structures with cool gas from the center of the cluster being dredged up in their wakes (Churazov et al. 2001; Gardini 2007; Revaz et al. 2008). This phenomenon is observed in the eastern arm of M87 (Forman et al. 2007) and in the dredging up of $H\alpha$ filaments behind AGN inflated bubbles in the Perseus cluster (Hatch et al. 2006).

The radio emission at 235 MHz is much more extended than the emission at 610 MHz and there is little overlap between the two frequencies (see Fig. 5). The lack of any detected emission at 610 MHz in the same region as the 235 MHz emission indicates that the radio spectrum must be very steep with a spectral index of $\alpha \gtrsim 1.6$. The absence of any 610 MHz emission in the 235 MHz radio lobes implies that the radio spectrum of the lobes must be fairly flat ($\alpha \lesssim 1.6$). There are two separate extended components in the 235 MHz observation. One of the components originates at the center of NGC 5044, passes through the southern cavity and then bends toward the west just behind the SE cold front (see Fig. 6). The bending is probably due to the streaming of gas behind the SE cold front. Beyond the SE cold front, the radio emission sharply bends toward the south, possibly due to the effects of buoyancy. While the cavities in NGC 5044 have a nearly isotropic distribution, Fig. 6 shows that all of the extended radio emission lies to the south and south-east. Fig. 6. also shows that no radio emission is detected in most of the X-ray cavities.

The GMRT observation at 235 MHz shows that there is a second detached radio lobe toward the south-east (see Figs. 5 and 6). The north-western edge of this radio lobe coincides with the SE cold front, suggesting that the relativistic material in the lobe was produced by an earlier radio outburst

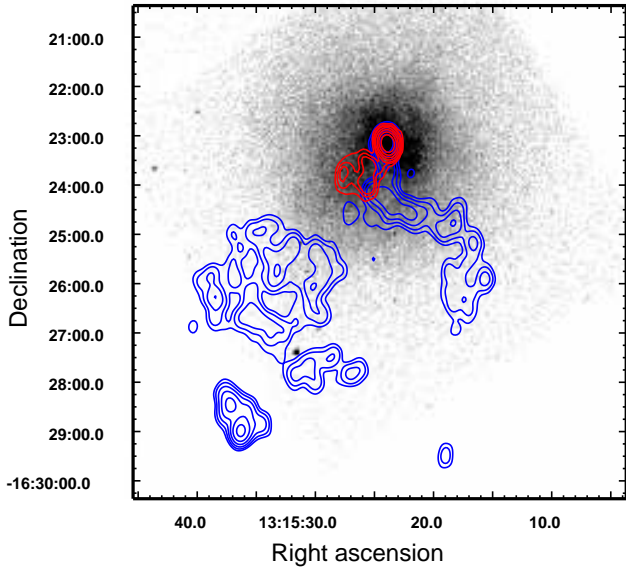


FIG. 5.— GMRT 610 MHz contours (red) and 235 MHz contours (blue) overlaid on the raw 0.3-2.0 keV ACIS image. The 610 MHz contours are the same as those shown in Fig. 4. For the 235 MHz data, the beam size is $22''$ by $16''$ and the lowest contour is shown at $3\sigma = 0.75$ mJy b^{-1} . The source in the bottom left corner is a background radio galaxy.

from NGC 5044 and that it is currently being compressed by the motion of NGC 5044 toward the south-east. The GMRT data thus appears to reveal 2 or possibly 3 separate radio outbursts. The youngest outburst can be identified with the 610 MHz emission and the oldest outburst with the detached radio lobe. The GMRT observation of NGC 5044 will be discussed in more detail in Giacintucci et al. (2009b).

3.3. Point Sources

The central AGN and other hard X-ray point sources are easily seen in the raw 2.0-7.0 keV ACIS image (see Fig. 7). Using the CIAO tool *wavdetect*, 12 point sources, in addition to the central AGN, are detected within the central $4'$ by $4'$ (44 by 44 kpc) region with an unabsorbed 2.0-7.0 keV flux limit of 1.26×10^{-15} erg cm^{-2} s^{-1} (assuming a power-law spectrum with an index of $\Gamma = 1.4$). The hard X-ray band log N-log S relation for background point sources given by Moretti et al (2003) predicts 7 ± 3 point sources above this flux limit within this region, so there is not a significant excess of point sources over this region. However, within the central 15 kpc, there are 8 detected point sources in addition to the central AGN and the predicted background number is 2.3 ± 1 . Thus, some of these point sources are probably low-mass X-ray binaries associated with NGC 5044. Assuming these 8 point sources are at the distance of NGC 5044, gives 2-7 keV luminosities between $3.3 - 15.3 \times 10^{38}$ erg s^{-1} , which are typical luminosities for the most luminous LMXBs in early-type galaxies (e.g., Sarazin, Irwin & Bregman 2001; Kraft et al. 2001; Kim & Fabbiano 2004; David et al. 2006; Brassington et al. 2008).

4. TEMPERATURE, PRESSURE AND ENTROPY MAPS

Most of the X-ray emission from 1 keV groups and early-type galaxies arises from L shell transitions from Fe with ionization states from Fe XIX (Ne-like) through Fe XXIV (He-like). With CCD spectral resolution, these L-shell lines are blended into a single feature between approximately 0.7 and 1.2 keV. When fitting the spectra of gas with temperatures of approximately 1 keV, the temperature is primarily determined

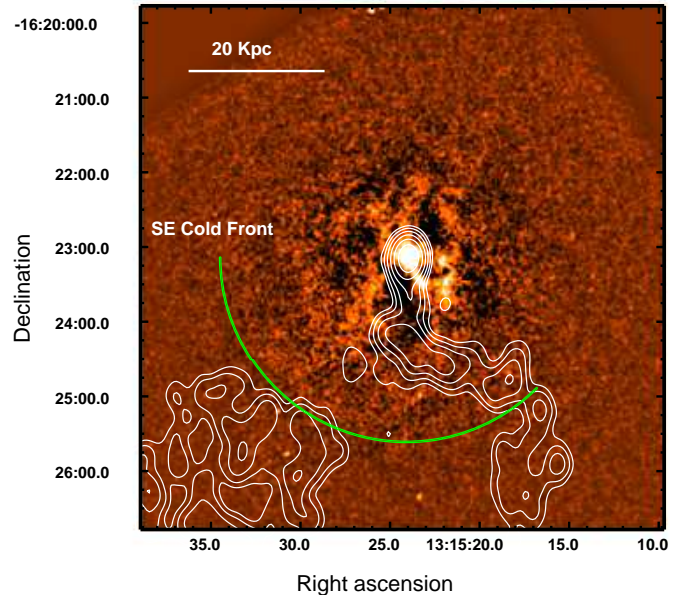


FIG. 6.— GMRT 235 MHz contours overlaid on the unsharp masked image. The contours are the same as shown in Fig. 5. Also shown is the location of the SE cold front.

by the energy centroid of the blended Fe-L lines. This results from the shift in the dominant ionization state of Fe from Fe XIX in 0.5 keV gas to Fe XXIV in 1.2 keV gas. Since Li-like Fe is the highest ionization state of Fe that can produce L shell lines, the mean photon energy of the blended L shell lines is independent of temperature above 1.2 keV. To determine the correlation between mean photon energy in the 0.7-1.2 keV energy band and gas temperature, we generated a series of XSPEC simulated spectra based on an absorbed vaped model with temperatures between 0.5 and 1.5 keV. These simulations assume galactic absorption ($N_{gal} = 4.94 \times 10^{20}$ cm^{-2}) and the redshift of NGC 5044. The emission between 0.7 and 1.2 keV also contains some emission from O, Ne and Mg, however, assuming solar abundances for all elements, 93% of the emission in this energy band arises from Fe in 1 keV gas, so the mean photon energy is essentially independent of the assumed abundance ratios. Fig. 8 shows that there is a linear correlation ($kT = -4.61 + 5.88 < E >$) between temperature and mean photon energy up to temperatures of approximately 1.2 keV.

Using the linear correlation shown in Fig. 8 between mean photon energy and temperature between 0.5 and 1.2 keV (which is approximately the maximum observed temperature in NGC 5044), we have generated a high resolution temperature map of NGC 5044 (see Fig. 9). The advantage of this method is that far fewer counts are required to compute the mean photon energy than that required for a full spectral analysis. Also, the derived temperature is independent of the Fe abundance and abundance ratios. The temperature map shown in Fig. 9 was derived by first applying a 3σ adaptive smoothing to the raw image in the 0.7-1.2 keV band. The same kernel was then used to adaptively smooth an image of the summed photon energy in the 0.7-1.2 keV band. Dividing these images produces an image of the mean photon energy and the temperature can then be computed from the linear relation shown in Fig. 8. The primary source of uncertainty in the estimated temperatures is the discrepancy between the linear function used in Fig. 8 and the mean photon energies computed from the XSPEC simulations and corresponds to about 2-3%.

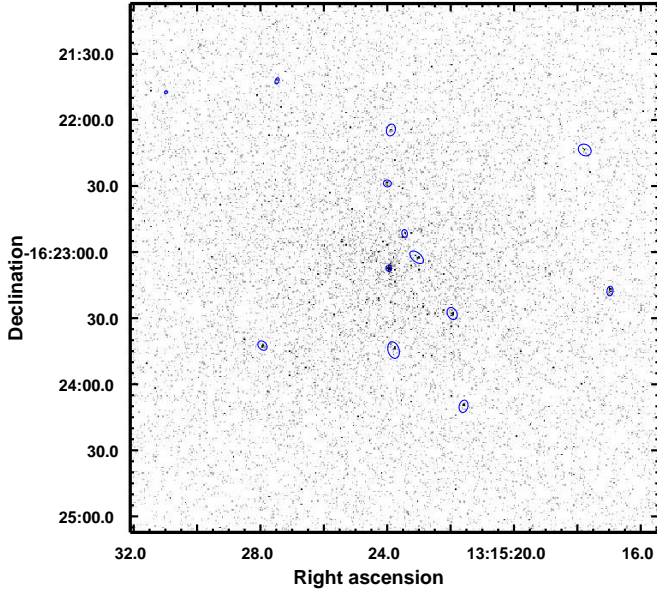


FIG. 7.— Raw 2.0-7.0 keV ACIS image of the central 4' by 4' region of NGC 5044. All detected point sources are identified with elliptical contours.

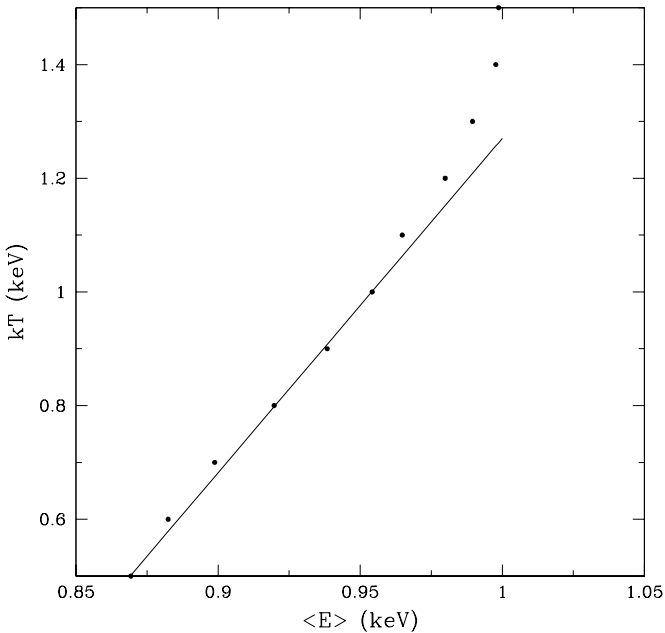


FIG. 8.— Correlation between gas temperature and mean photon energy in the 0.7-1.2 keV energy band as derived from XSPEC simulations.

Fig 9. shows that there is a great deal of structure in the gas temperature within the central 50 kpc of NGC 5044. There is a clear extension of the coolest gas toward the south-east in the direction of the SE cold front (shown by the white arc in Fig. 9) and the SE spiral. A hardness ratio image of the ROSAT observation of NGC 5044 also showed that the X-ray softest emission in NGC 5044 was contained in a "tear-drop" shaped feature extending toward the south-east (David et al. 1995). The SE cold front clearly bounds most of the cool central gas, however, the cool gas in the SE spiral can be detected out to approximately 50 kpc from the AGN, which is beyond any detected radio emission. All of the bright filaments visible in Figs. 1 and 2 have cooler gas compared to the surrounding regions. Higher temperatures are observed in the cavities, probably due

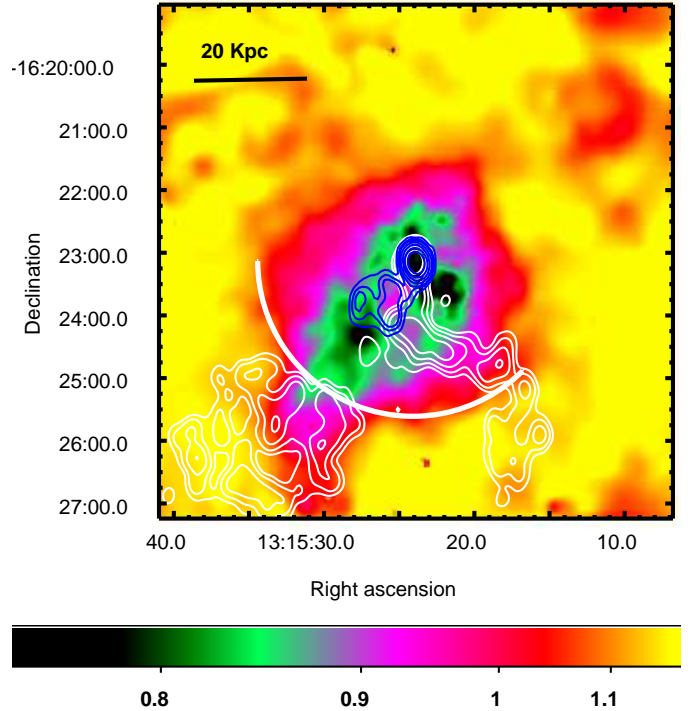


FIG. 9.— Temperature map of the central region of NGC504. The color coded gas temperatures are shown on the color bar. Also shown are the GMRT contours at 610 MHz (blue) and 235 MHz (white) and the location of SE cold front.

to foreground and background emission from hotter gas. The fact that the colors in the temperature map at the locations of the cavities are red (0.9-1.0 keV) and not yellow (1.1-1.2 keV), indicates that these cavities are not highly elongated along the line-of-sight. The 235 MHz and 610 MHz radio contours show that the AGN is located at the north-east end of the cool SW filament.

The correspondence between gas temperature and enhancement in the X-ray surface brightness is shown in Fig. 10. This figure plots the gas temperature, as determined from the temperature map, and the value in the unsharp masked image for every point in the two images. Positive values in the unsharp masked image correspond to enhancements in the surface brightness and negative values correspond to depressions. Below temperatures of 0.9 keV, Fig. 10 shows that there is a general trend for enhanced regions to contain cooler gas and for depressions to contain hotter gas, suggesting that these regions are in rough pressure equilibrium. One of the more surprising results in Fig. 10 is the lack of significant enhancements or depressions in gas hotter than 0.9 keV. Based on the temperature profiles presented below, this corresponds to a radial distance of approximately 20-30 kpc. We also produced the same plot derived from unsharp masked images generated from a range of smoothing lengths and found the same result. The trend in Fig. 10 shows that there are no cavities or filaments of the same spatial scale or amplitude as those seen in the central region beyond the SE cold front. This suggests that AGN inflated, buoyantly rising cavities with sizes similar to those currently seen in the center of NGC 5044 are disrupted, or prevented from buoyantly rising beyond the central 30 kpc.

A pressure map of the central region of NGC 5044 was generated from the product of the temperature map shown in Fig. 9 and a density map. The density map was derived from the

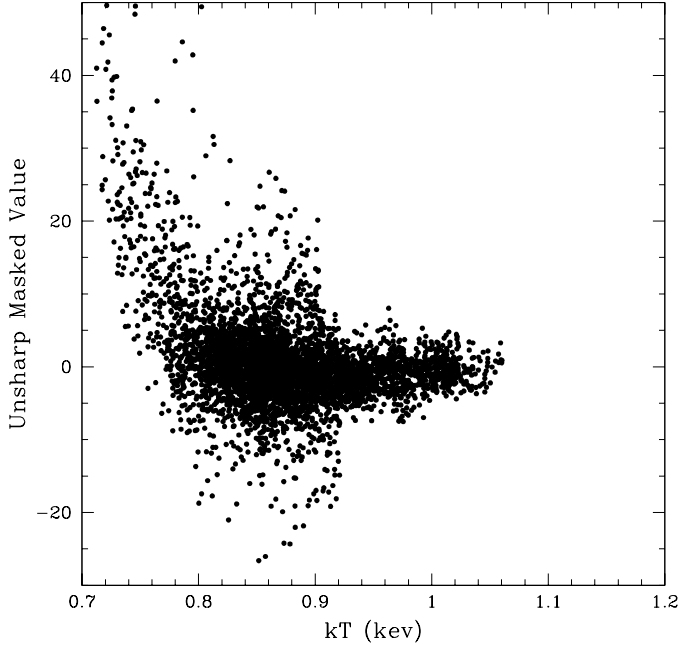


FIG. 10.— Comparison between the gas temperature (determined from the temperature map in Fig. 9) and the enhancement in the X-ray surface brightness based on the value in the unsharp masked image shown in Fig. 3.

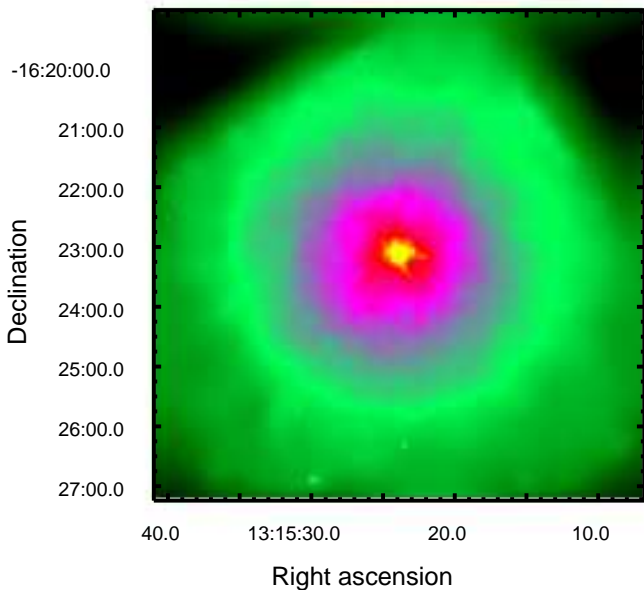


FIG. 11.— Gas pressure map of the central region of NGC 5044.

same 3σ adaptively smoothed image used to calculate the temperature map assuming $n_e \propto (\Sigma/r)^{1/2}$, where Σ is the surface brightness in a given region and r is the distance between the given region and the center of the group. The electron density was normalized at a radial distance of 100 kpc based on the results of a deprojected spectroscopic analysis. The deprojected spectral analysis will be presented in a subsequent paper (David et al. 2009). Even though there is significant structure in the ACIS image and temperature map, the resulting pressure map shown in Fig. 11 is nearly azimuthally symmetric with only a few weak features. To enhance any pressure residuals, we computed an azimuthally averaged pressure map based on

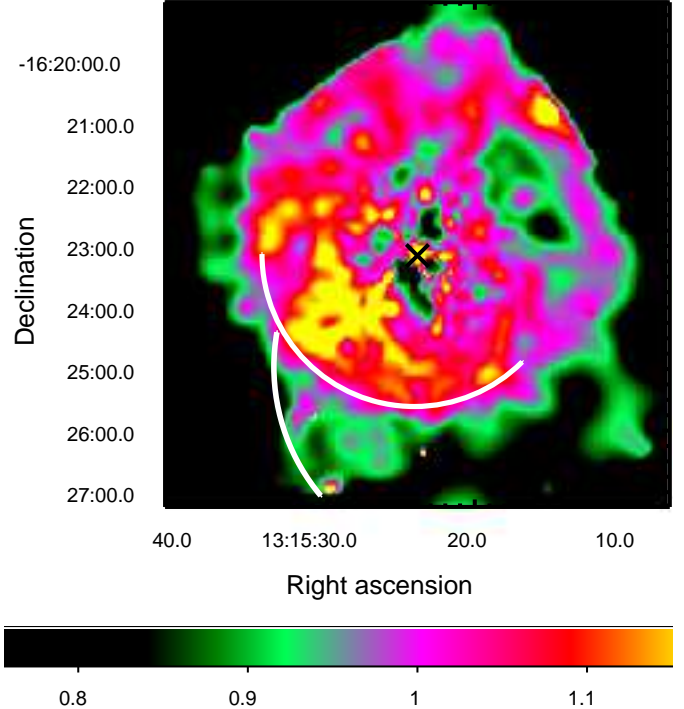


FIG. 12.— Pressure residual map of the central region of NGC 5044. The positions of the SE cold front and SE spiral are shown as white arcs and the location of the central AGN is indicated with a "X". The relative magnitude of the pressure residuals are shown on the color bar.

the azimuthally averaged pressure profile derived from the pressure map. A pressure residual map (see Fig. 12) was then obtained by dividing the pressure map with the azimuthally averaged pressure map. Fig. 12 shows that the pressure is approximately 20% higher toward the south-east and 20% lower toward the north-west relative to the azimuthally averaged values. The outer edge of the high pressure region toward the south-east coincides with the SE cold front shown as a white arc in the Fig. 12, providing further evidence that this cold front is due to motion of NGC 5044 relative to the group gas.

An entropy map, where $S = kT/n_e^{2/3}$, was computed directly from the temperature and density maps (see Fig. 13). The overall shape of the entropy map is similar to the temperature map with the lowest entropy gas more extended in the direction of the SE cold front and spiral. Fig. 13 shows that the entropy gradient is the steepest near the SE cold front.

5. SURFACE BRIGHTNESS PROFILES

5.1. Azimuthally Averaged Profile

Emission from the NGC 5044 group was detected on all 5 CCDs that were turned on during the ACIS observation and data is available out to a radius of approximately $20'$ (220 kpc). Fig. 14 shows the background-subtracted and exposure corrected surface brightness profile in the 0.3-2.0 keV energy band including data from all 5 CCDs. The background for each CCD was determined using the method described in §2. Separate exposure maps were generated for each CCD at an energy corresponding to the mean source photon energy in the 0.3-2.0 keV energy band. The central point source is evident in the innermost bin of the surface brightness profile shown in Fig. 14, as are the inner cavities and a central power-law region extending out to approximately 3 kpc with a slope of ~ 0.3 . Even though

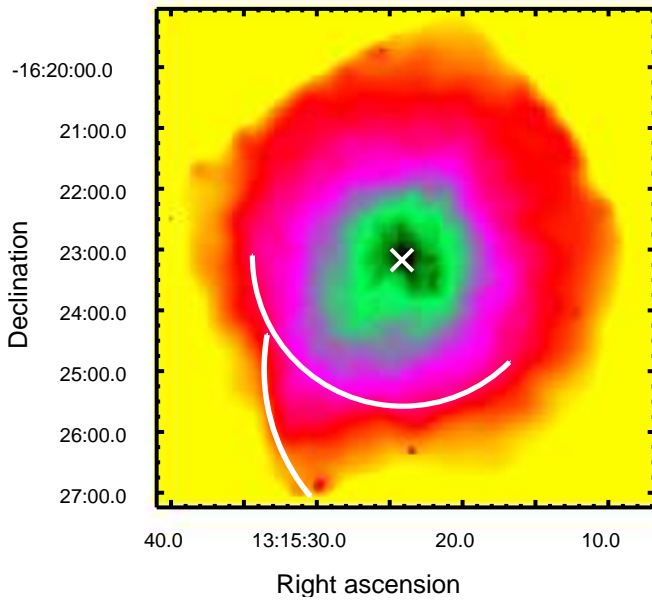


FIG. 13.— Entropy map of the central region of NGC 5044. The positions of the SE cold front and SE spiral are shown as black arcs and the location of the central AGN is indicated with a "X". The innermost contour is drawn at an entropy of 10 keV cm^2 and the contour levels increase in increments of 10 keV cm^2 .

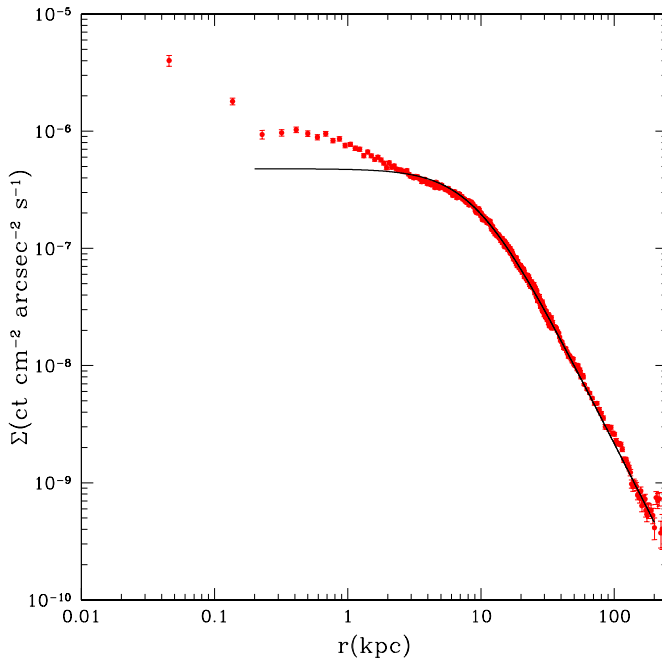


FIG. 14.— Azimuthally averaged, background-subtracted and exposure corrected 0.3-2.0 keV surface brightness profile of NGC 5044. The best fit β model is shown as a solid line.

there is significant substructure in the central region of NGC 5044, beyond 3 kpc, the azimuthally averaged surface brightness profile is remarkably smooth. We therefore fitted the 0.3-2.0 keV surface brightness profile beyond 3 kpc to the standard β model:

$$\Sigma(r) = \Sigma_0 \left[1 + \left(\frac{r}{r_0} \right)^2 \right]^{-3\beta+0.5}$$

and obtained $r_0 = 9.1 \pm 0.1 \text{ kpc}$ and $\beta = 0.541 \pm 0.001$ (1σ errors). The outer slope of the best-fit β model shown in

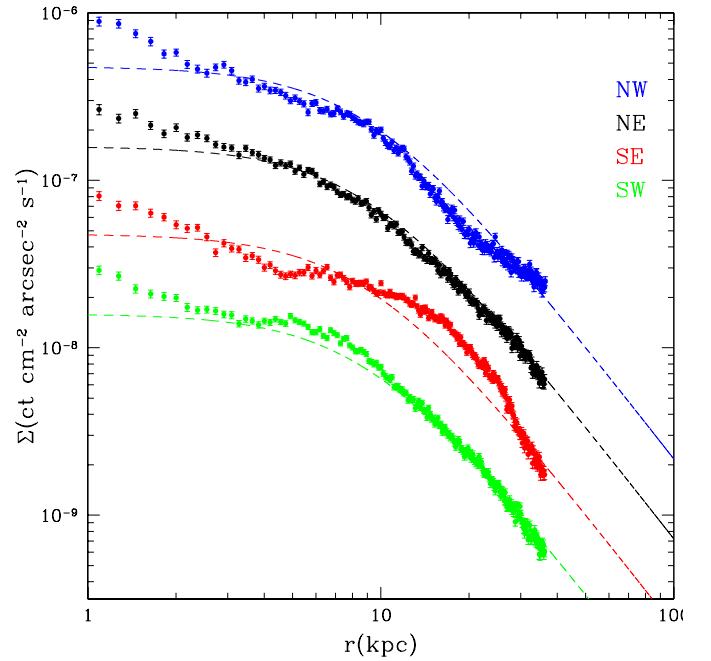


FIG. 15.— Background subtracted and exposure corrected 0.3-2.0 keV surface brightness profiles in 4 quadrants. The profiles are off-set for clarity of presentation. For comparison, the best-fit azimuthally average β model (shown in Fig. 14) is plotted as a dashed line.

Fig. 14 is in good agreement with the ROSAT PSPC analysis which included emission out to $40'$ ($\beta = 0.53$; David et al. 2001) and the XMM-Newton PN surface brightness profile fitted by Buote et al. (2003), who obtained $\beta = 0.52$.

5.2. Azimuthal Variations in the Surface Brightness Profile

We also generated background-subtracted and exposure corrected surface brightness profiles in the 0.3-2.0 keV energy band in 4 quadrants to a projected radius of 40 kpc, which is the full extent of the S3 chip (see Fig. 15). This figure shows that there are significant azimuthal variations in the surface brightness profile within the central 30 kpc (the location of the SE cold front). Beyond the SE cold front, all 4 surface brightness profiles are similar. The inner cavities show up as depressions in the surface brightness profiles within the central 10 kpc. Between 10 and 30 kpc, the surface brightness profiles toward the north-east and south-west (perpendicular to the direction of the SE cold front) closely follow the azimuthally averaged surface brightness profile. The south-east surface brightness profile is significantly higher than the azimuthally averaged value between 10-30 kpc, while the north-west surface brightness profile is significantly lower in this region. The SE cold front is clearly visible as a break in south-east surface brightness profile at approximately 30 kpc. There is also a break in the north-west surface brightness profile at 30 kpc in the opposite sense (i.e., shallow inner surface brightness and steep outer surface brightness). The azimuthal variations in the surface brightness profiles between 10 and 30 kpc are probably due to the sloshing motion of NGC 5044 toward the south-east.

To further search for any features in the ACIS image of NGC 5044, we computed surface brightness profiles within several concentric annuli as a function of position angle (see Fig. 16). The SE spiral shows up as a spike in the surface brightness profiles at a position angle of approximately 140° and is clearly evident to the edge of the S3 chip. There is also a smaller amplitude spike in all 4 surface brightness profiles shown in

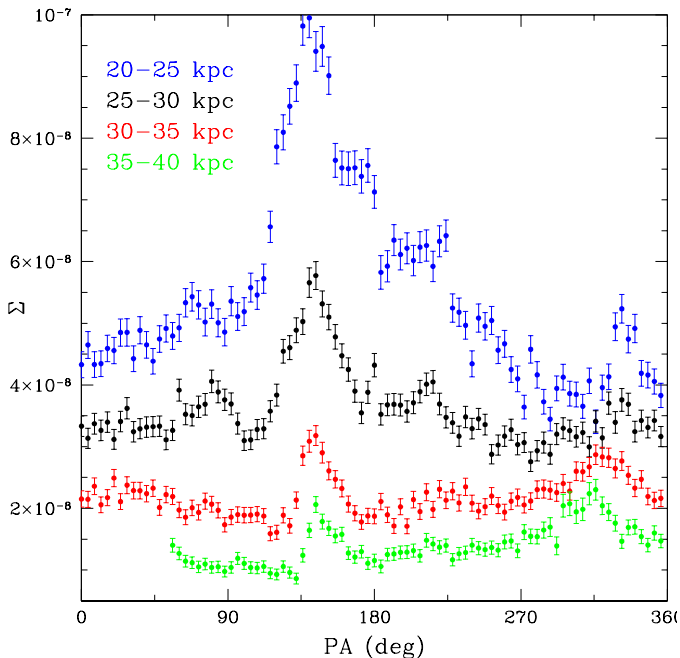


FIG. 16.— Background subtracted and exposure corrected 0.3-2.0 keV surface brightness profiles within several annular regions vs. position angle (measured counter clockwise from due north).

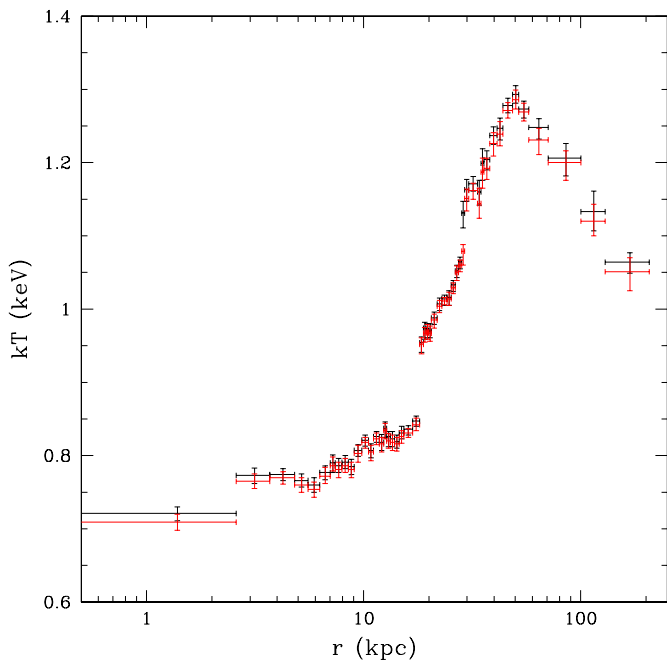


FIG. 17.— Azimuthally averaged projected temperature profile. The temperatures are derived by fitting the spectra in the 0.5-5.0 keV energy band to an absorbed single temperature model (black data points) and an absorbed single temperature plus power-law model (red data points).

Fig. 16 at a position angle of approximately 325° . This NW spiral is only marginally visible in the raw image shown in Fig. 2, but is quite evident in Fig. 16.

6. PROJECTED GAS TEMPERATURE PROFILES

Based on the surface brightness profile, we extracted a set of spectra within concentric annuli with 10,000 net counts per spectrum. The total net counts are based on the sum of the counts on all 5 chips. Source spectra, background spectra, photon weighted response files and photon weighted effective area

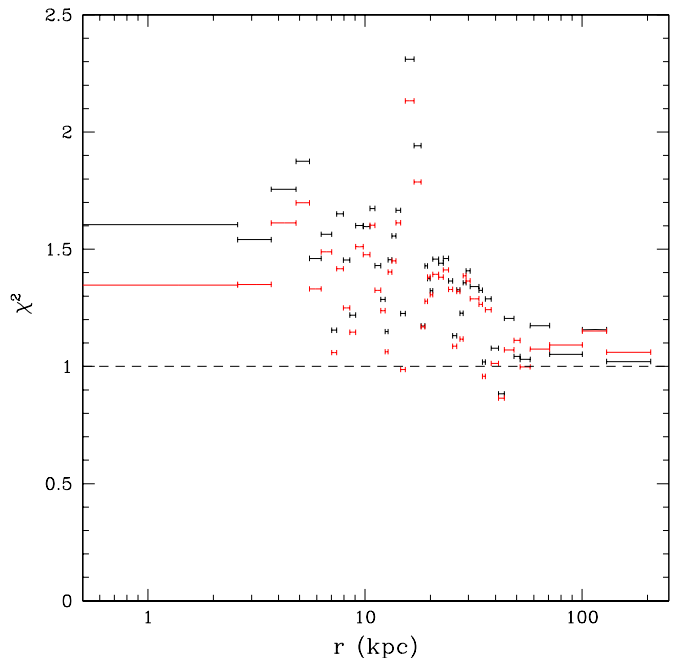


FIG. 18.— Reduced χ^2 for the azimuthally averaged spectra fit to an absorbed single temperature model (black data points) and an absorbed single temperature plus power-law model (red data points).

files were generated for each region after excising the emission from point sources (i.e., point sources detected by *wavdetect* in the 0.3-2.0 and 2.0-7.0 keV energy bands) using the CIAO task *specextract*. The background spectra are extracted from the normalized blank sky data sets discussed in §2. Beyond $200''$ (the region fully covered by the S3 chip), the spectra from different chips are fit simultaneously. Each spectrum was fitted in the 0.5-5.0 keV energy band to an absorbed vpec thermal plasma model and an absorbed vpec plus power-law model with the index frozen at $\Gamma = 1.4$ to account for the emission from unresolved LMXBs. The hydrogen column density was fixed to the galactic value, $N_H = 4.94 \times 10^{20} \text{ cm}^{-2}$. We adopt the abundance table of Grevesse & Sauval (1998) in our spectral analysis and treat O, Ne, Mg, Si, S, Ar and Fe as free parameters with the Ni abundance linked to the Fe abundance and the Ca abundance linked to the Ar abundance.

6.1. Azimuthally Averaged Projected Temperature profile

From our moderately deep Chandra observation, we are able to derive a high spatial resolution temperature profile of NGC 5044 (see Fig. 17). The temperatures derived from a single thermal plasma model and a thermal plus power-law model are fully consistent (compare the black and red data points in Fig. 17). Within the 0.5-5.0 keV energy band, 85% of the detected photons have energies below 1.5 keV for 1 keV gas, so the spectral fits are heavily weighted by the soft thermal emission and are not significantly affected by the harder emission from unresolved LMXBs. The overall temperature profile shown in Fig. 17 is similar to that observed in other groups with a positive temperature gradient at small radii, a peak temperature at approximately 50 kpc, and a declining temperature profile at larger radii (e.g., Finoguenov et al. 2007; O'Sullivan et al. 2009). Within the central 10 kpc, the azimuthally averaged temperature is nearly isothermal with temperatures between 0.70-0.85 keV (consistent with the temperature map shown in Fig. 9). There are two sharp temperature jumps at 20 and 30 kpc

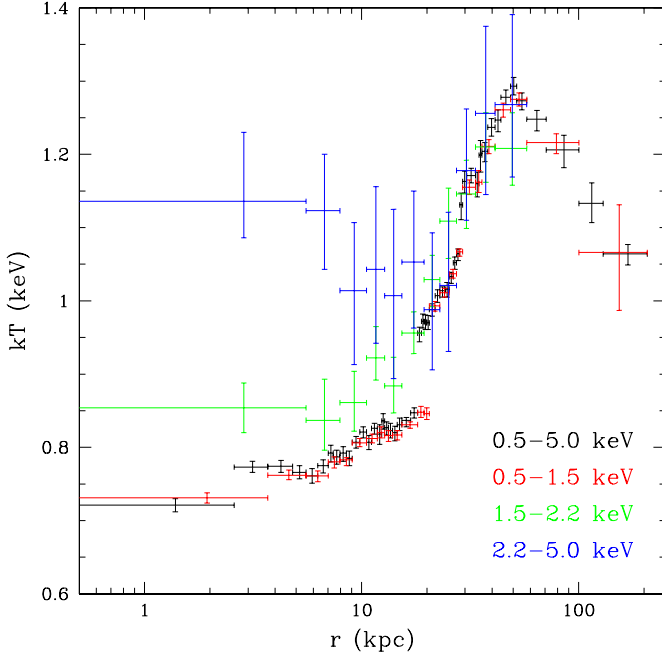


FIG. 19. — Azimuthally averaged projected temperature profile derived from fitting the spectra in 4 different energy bands: 1) a broad energy band from 0.5-5.0, 2) a soft energy band from 0.5-1.5 keV which contains mostly emission from Fe-L lines, 3) an energy band from 1.5-2.2 keV which contains line emission from H-like and He-like Si, and 4) a hard energy band from 2.2-5.0 keV which contains some continuum plus line emission from S, Ar and Ca.

seen in Fig. 17. The outer temperature jump corresponds to the SE cold front. The inner temperature jump is primarily due to the non-azimuthal structure of the central gas temperature (see the temperature map in Fig. 9 and §6.2). Within 20 kpc, the spherical annuli only contain emission from the coolest gas. Beyond this radius, the spherical annuli also contain some emission from hotter gas. The reduced χ^2 values for the spectral fits are shown in Fig. 18. While the inclusion of a power-law component in the spectral analysis does not affect the derived gas temperatures, it does significantly reduce the χ^2 value in most spectra. For example, applying a F-test on the spectral fitting results of the innermost 5 annuli shows that the improvement in the fits is significant at more than 98% in each case. Fig. 18 shows that single temperature fits are reasonably acceptable beyond 50 kpc, which corresponds to the peak of the temperature profile and the extent of the cool SE spiral. The degradation in the spectral fits within this region is primarily due to projection effects, azimuthal variations in the gas temperature and the presence of multi-phase gas, as can be seen in the temperature map shown in Fig. 9.

We also fitted the azimuthally averaged spectra to an absorbed thermal plasma model in three additional energy bands to determine the influence of the emission from unresolved LMXBs: 1) a soft energy band from 0.5-1.5 keV which contains mostly Fe-L emission lines plus some weaker emission from O, Ne and Mg, 2) an energy band from 1.5-2.2 keV, which contains emission lines from He-like and H-like Si, and 3) a harder energy band from 2.2-5.0 keV, which contains mostly continuum emission plus emission lines from S, Ar and Ca (see Fig. 19). For the soft energy band we used a set of spectra with 20,000 net counts each and for the harder energy bands we used a set of spectra with 40,000 net counts each. Since most of the photons in the 0.5-5.0 keV energy band have energies below 1.5 keV, the temperature profile derived in the broad and soft

energy bands are in good agreement. The temperature profiles derived from the Si line ratio and the hard energy band also agree with the temperature profile derived from the broad and soft energy bands beyond 30 kpc. The influence of the LMXBs on the derived gas temperatures is most notable in the hard energy band within the central 30 kpc.

To unambiguously determine if the harder spectral component in the center of NGC 5044 arises from an extra component of hotter gas or LMXBs, we fitted the 1.5-7.0 keV emission within the central 8 kpc to a single temperature model, a two-temperature model (with the abundances linked) and a single temperature plus power-law model (see the results in Table 1). As can be seen in Table 1, the thermal plus power-law model provides the best fit to the emission within the central 8 kpc. In addition, the best-fit temperature is consistent with the central gas temperature derived above and the best-fit power-law index is consistent with the characteristic power-law emission from LMXBs. The unabsorbed 2.0-7.0 keV flux of the power-law component is $F(2-7 \text{ keV}) = 6.6 \times 10^{-14} \text{ erg cm}^{-2} \text{ s}^{-1}$. Combining this with the 2.0-7.0 keV flux of the resolved point sources within the central 8 kpc gives a total 2.0-7.0 keV flux and luminosity for the LMXBs of $F(2-7 \text{ keV}) = 7.5 \times 10^{-14} \text{ erg cm}^{-2} \text{ s}^{-1}$ and $L(2-7 \text{ keV}) = 4.5 \times 10^{39} \text{ erg s}^{-1}$. The 2.0-7.0 keV flux from the LMXBs within the central 8 kpc is 17% of the total flux from the galaxy. In David et al. (2006), we showed that there is a strong correlation between the total 0.5-2.0 keV luminosity of the LMXBs in early-type galaxies and the K-band luminosity of the galaxies. An analysis of the 2MASS K-band image of NGC 5044 gives $m_K = 8.00$ and $L_K = 1.96 \times 10^{11} L_{K\odot}$ within the central 8 kpc. Using eq. (1) in David et al. (2006), we find a predicted luminosity of $L(0.5-2.0 \text{ keV}) = 4.1 \times 10^{39} \text{ erg s}^{-1}$. A power-law spectral model with $\Gamma = 1.4$ gives $L(2-7 \text{ keV}) = 8.1 \times 10^{39}$, which is consistent with the observed 2-7 keV luminosity, given the observed scatter in the relationship. This analysis shows that the harder X-ray component in the center of NGC 5044 is most likely due to unresolved LMXBs and not a second component of hotter gas. In general, since the X-ray emitting gas has a more extended distribution than the stars and LMXBs in early-type galaxies and the gas is the coolest in the center, the harder X-ray emission from LMXBs should be the most prevalent in the center of these galaxies.

6.2. Azimuthal Variations in Projected Temperature Profiles

The projected temperature profiles within 4 quadrants out to 40 kpc (the field of view of the S3 chip) are shown in Fig. 20. The SE cold front shows up as a sharp temperature jump in the south-east temperature profile at a radius of 30 kpc. Interior to the SE cold front, the gas is essentially isothermal. The north-west temperature profile shows a temperature jump at 20 kpc which coincides with the break in the north-west surface brightness profile (see Fig. 15). There is also a significant temperature jump in the south-west temperature profile at a radius of 20 kpc, but there is no obvious break in the surface brightness at this location (see Fig. 15). This temperature jump is likely due to non-azimuthal variations in the gas temperature within the south-west quadrant. A further analysis of the temperature map shows that the temperature varies by 15% at a radius of 20 kpc within the SW quadrant (i.e., between position angles of 180 and 270°). There are also weaker temperature jumps in the north-east and north-west directions at approximately 14 kpc.

TABLE 1
SPECTRAL ANALYSIS OF THE INNER 8 KPC

| Model | kT_c (keV) | kT_h (keV) | Γ | χ^2/DOF |
|--------------------|------------------|------------------|------------------|--------------|
| WABS*VAPEC | 0.90 (0.87-0.93) | - | - | 167/124 |
| WABS*(VAPEC+VAPEC) | 0.55 (0.45-0.67) | 1.26 (1.14-1.46) | - | 152/122 |
| WABS*(VAPEC+POW) | 0.83 (0.79-0.89) | - | 1.27 (0.79-1.87) | 146/122 |

Notes: Spectral analysis of the emission from the central 8 kpc. The spectrum was fitted to a single temperature model, a two-temperature model and a single temperature plus power-law model. The best-fit temperature in the single temperature model and the best-fit lower temperature in the two-temperature model are given by kT_c . The best-fit higher temperature in the two-temperature fit is given by kT_h . The best-fit index in the single temperature plus power-law fit is given by Γ . The last column gives the χ^2 per degree of freedom. All error bars are given at the 90% confidence limit.

These jumps are also probably due to non-azimuthal temperature variations within these quadrants.

The presence of cool gas in the SE and NW spirals can best be shown by plotting the azimuthal variations in gas temperature within concentric annuli between 20 and 40 kpc from the center of NGC 5044 (see Fig. 21). This figure shows two sharp temperature drops at position angles of 135° and 315° , which are coincident with the SE and NW spirals seen in the surface brightness profiles shown in Fig 16. Within the inner annulus, there is also a broader dip in gas temperature between $PA=0$ and $PA=270^\circ$, due to the greater extent of cool gas in the south-east direction (see the temperature map in Fig. 9).

7. SPECTRAL ANALYSIS OF THE AGN, CAVITIES AND FILAMENTS

7.1. The AGN and Innermost Gas

To deduce the spectral properties of the AGN in NGC 5044, we extracted a spectrum from within a $1.2''$ (220 pc) radius region centered on the AGN. Table 2 shows that the spectrum is poorly fitted with a thermal or power-law model, but is well fitted with a thermal plus power-law model. The best-fit temperature in the thermal plus power-law model is consistent with the central gas temperature shown in the temperature map (see Fig. 9) and temperature profile (see Fig. 17). We also allowed the hydrogen column density to vary in the fitting process, but there is no evidence for excess absorption above the galactic value. The best-fit power-law index in the two component model is also quite typical of AGN. Based on the best-fit thermal plus power-law model, the unabsorbed 0.5-5.0 keV flux and luminosity of the AGN are 1.98×10^{-14} erg s^{-1} cm^{-2} and 3.57×10^{39} erg s^{-1} and the bolometric X-ray luminosity is 6.64×10^{39} erg s^{-1} . The expected bolometric X-ray luminosity of the LMXBs based on the K-band luminosity of the galaxy within the central 220 pc is 3.3×10^{37} erg s^{-1} , which is less than 1% of the total luminosity of the power-law component within this region. The central radio point source was detected in our GMRT observations at frequencies of 235 MHz, 327 MHz and 610 MHz, with flux densities of 35 ± 2 mJy, 32 ± 2 mJy and 30 ± 2 mJy, respectively (Giacintucci et al. 2009). Integrating the radio flux density between 5 MHz and 10 GHz, assuming $S_\nu \propto \nu^{-\alpha}$ with $\alpha = 0.16$ gives a radio luminosity of $L_R = 4.1 \times 10^{38}$ erg s^{-1} . This shows that the radiative efficiency of the AGN in the radio band is only 6% of that in the X-ray band. Using a stellar velocity dispersion of $\sigma_* = 237$ km s^{-1} for NGC 5044 (which is the average of 4 measurements listed in HyperLeda) and the relation between stellar velocity dispersion

and central black hole mass in Gebhardt et al. (2000), gives a

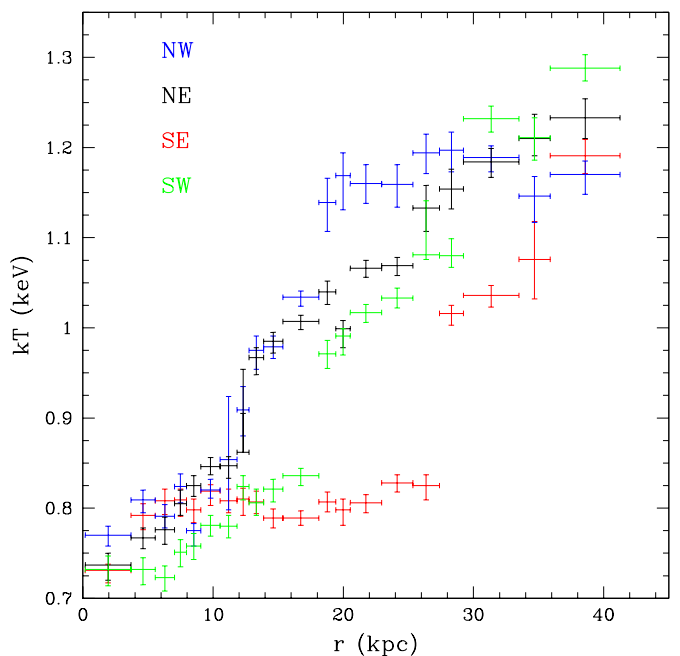


FIG. 20.— Projected temperature profile within 4 quadrants. The temperatures are derived by fitting the spectra in the 0.5-5.0 keV energy band to an absorbed single temperature plus power-law model.

central black hole mass of $M_{bh} = 2.27 \times 10^8 M_\odot$. This gives a ratio between the bolometric and Eddington luminosity of $L_{bol}/L_{Edd} = 2.3 \times 10^{-7}$.

The bolometric X-ray luminosity of the gas within the central 220 pc is 1.56×10^{39} erg s^{-1} based on the best-fit thermal plus power-law spectral model. Using the best-fit emission measure of the thermal component, assuming a uniform gas density within the central 220 pc, gives a density of $n_e = 0.21$ cm^{-3} and a total gas mass of $M_{gas} = 2.64 \times 10^5 M_\odot$. The isobaric cooling time of the gas is $t_c = 5kTM_{gas}/(2\mu m_p L_{bol}) = 3.5 \times 10^7$ yr. Alternatively, if we assume the gas density follows a power-law profile given by $n_e \propto r^{-0.8}$, consistent with the density distribution determined from a deprojected spectral analysis (David et al. 2009), we obtain $n_e = 0.14 (r/r_0)^{-0.8}$ cm^{-3} , with $r_0 = 220$ kpc.

The Bondi accretion radius of the central black hole is $R_a = GM_{bh}/c_a^2$, where c_a is the adiabatic sound speed at the accretion radius. Using a gas temperature of 0.75 keV gives $R_a = 4.9$ pc. The Bondi accretion rate is given by

TABLE 2
SPECTRAL ANALYSIS OF THE AGN

| Region | Model | kT (keV) | Γ | χ^2/DOF |
|--------|-----------------|------------------|------------------|--------------|
| AGN | WABS*APEC | 2.40 (1.39-3.34) | - | 53.1/17 |
| AGN | WABS*POW | - | 1.95 (1.79-2.10) | 53.8/18 |
| AGN | WABS*(APEC+POW) | 0.83 (0.75-1.02) | 1.44 (1.04-1.74) | 16.1/15 |

Notes: Spectral analysis of the emission from the central $1.2''$ (220 pc) region. The spectrum was fitted to a thermal plasma model, a power-law model and a thermal plus power-law model. The last column gives the χ^2 per degree of freedom. All error bars are given at the 90% confidence limit.

TABLE 3
SPECTRAL ANALYSIS OF THE FILAMENTS AND CAVITIES

| Region | Model | kT (keV) | χ^2/DOF |
|-------------|------------------|------------------|--------------|
| SE filament | WABS*(APEC+POW) | 0.83 (0.82-0.84) | 142/90 |
| SE filament | WABS*(VAPEC+POW) | 0.79 (0.78-0.80) | 108/85 |
| SW filament | WABS*(APEC+POW) | 0.70 (0.68-0.71) | 89.0/75 |
| SW filament | WABS*(VAPEC+POW) | 0.65 (0.64-0.66) | 69.3/70 |
| NE cavity | WABS*(APEC+POW) | 0.81 (0.80-0.82) | 72.3/65 |
| NE cavity | WABS*(VAPEC+POW) | 0.81 (0.79-0.83) | 59.1/60 |
| S cavity | WABS*(APEC+POW) | 0.84 (0.83-0.85) | 139/88 |
| S cavity | WABS*(VAPEC+POW) | 0.82 (0.80-0.84) | 114/83 |
| SW cavity | WABS*(APEC+POW) | 0.78 (0.77-0.79) | 68.6/70 |
| SW cavity | WABS*(VAPEC+POW) | 0.73 (0.71-0.75) | 42.1/65 |
| NW cavity | WABS*(APEC+POW) | 0.82 (0.81-0.84) | 142/74 |
| NW cavity | WABS*(VAPEC+POW) | 0.78 (0.76-0.80) | 87.1/69 |

Notes: Spectral analysis of the filaments and cavities shown in Fig. 22. The last column gives the χ^2 per degree of freedom. All error bars are given at the 90% confidence limit.

$\dot{M}_B = 4\pi R_a^2 \rho(R_a) c_a$. The greatest uncertainty in this

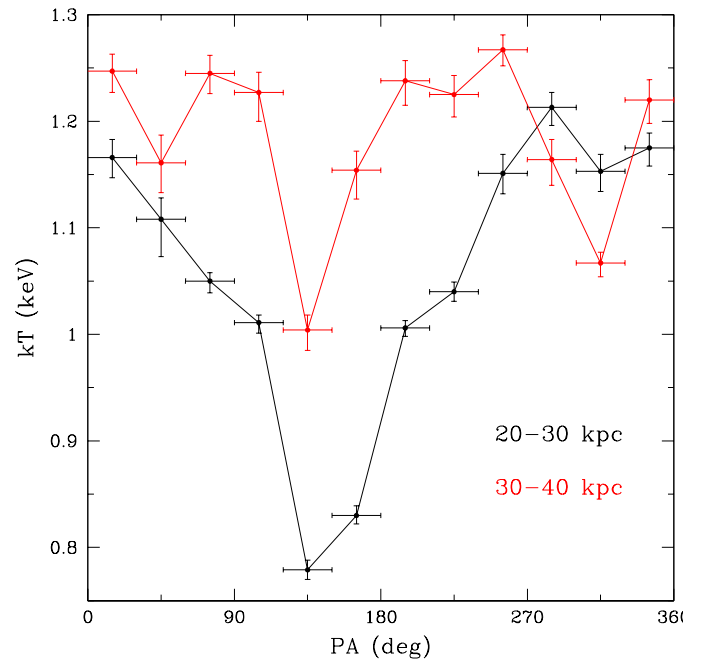


FIG. 21.— Projected temperature profile within two annular regions vs. position angle (measured counter clockwise from due north).

expression is the gas density at the Bondi radius. Even in the nearby NGC 5044 group, an extrapolation over a factor of 40 in radius is required to estimate the density at R_a . If the gas is isothermal and the density follows the same power-law expression given above, then $\dot{M}_B = 0.011 M_\odot \text{ yr}^{-1}$. If the X-ray luminosity of the AGN is powered by Bondi accretion, the resulting efficiency ($\epsilon = L_{\text{bol}}/(\dot{M}_B c^2)$) is 1.1×10^{-5} , which is typical of the radiatively inefficient AGN in early-type galaxies (Loewenstein et al. 2001; Di Matteo et al. 2003; David et al. 2005).

7.2. Cavities and Filaments

Spectra were extracted from the cavities and filaments using the regions shown in Fig. 22 and fitted to absorbed *apec* and *vapec* models in the 0.5-5.0 keV energy band. A power-law component was added in both cases to account for the emission from unresolved X-ray binaries with the power-law index frozen at $\Gamma = 1.4$. Table 3 shows that the *apec* model provides a poor fit to the spectra extracted from both the cavities and filaments. A significant improvement is obtained with the *vapec* model indicating that either the abundance ratios differ from those in the abundance table of Grevesse & Sauval (1998), or the gas is multi-phase (especially as seen in projection),

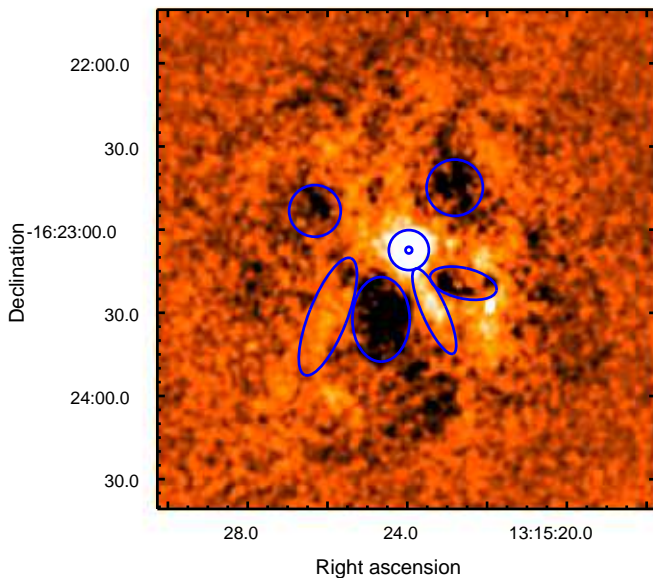


FIG. 22.— Regions used to extract spectra for the cavities, AGN and filaments (see Table 3).

and that different lines are being excited by different temperature gas. However, as is also evident from the temperature map (in which the gas temperature is derived solely from the centroid of the Fe-L lines), the cavities have higher temperatures than the filaments, but only by 0.05-0.1 keV. Both the temperature map and temperature profile show that the gas is nearly isothermal within the central 10 kpc. Most of the cavities are only a few kpc in extent, so the gas that was displaced likely had a temperature similar to the surrounding gas seen in projection. The coolest gas within the central region of NGC 5044 is located within the SW filament with $kT = 0.65$ keV (see Table 3). This is also evident in the temperature map derived from the earlier 20 ksec ACIS observation presented by Gastaldello et al. (2008).

We also searched for evidence of hot thermal gas entrained within the cavities by extracting a spectrum of the combined emission from all 4 cavities shown in Fig. 22. The extracted spectrum shows no evidence for any Fe-K α emission, which would be an unambiguous sign of shocked hot gas in a group of galaxies. The net count rate between 5 and 7 keV is actually consistent with zero with a 3σ upper limit of 1.1×10^{-4} ct s^{-1} . If we scale the expected emission from X-ray binaries according to the K-band luminosity of the galaxy within the 4 cavities we find a predicted 5-7 keV count rate from X-ray binaries of 1.0×10^{-4} ct s^{-1} , which is just below our 3σ upper limit. Since the projected cavity spectrum contains thermal emission from gas with temperatures between 0.8 and 1.4 keV, and since we are only interested in detecting gas hotter than that encountered along the line-of-sight, we fitted the spectrum in the 2.5-5.0 keV energy band to an absorbed *vapec* plus power-law model (to account for the emission from unresolved LMXBs) and obtained a best-fit temperature of $kT = 0.90 \pm 0.30$ keV (90% errors), which is consistent with emission from ambient gas along the line-of-sight.

To place constraints on the amount of hot gas entrained within the cavities, we computed the predicted count rate in the 5-7 keV energy band for gas in pressure equilibrium with the surrounding medium assuming a solar abundance of Fe (see Table 4). This table shows that the predicted count rates for gas hotter than 2 keV are all well below the 3σ upper limit and the count rate expected from unresolved LMXBs. Thus, we cannot exclude the presence of gas with temperatures as low as 2 keV in pressure equilibrium within these cavities.

8. DISCUSSION

8.1. Interaction of the Radio Plasma with the Hot Gas

NGC 5044 hosts many small X-ray cavities with a nearly isotropic distribution and one larger cavity toward the south. The smaller cavities are all radio quiet, even at low frequencies (sensitivity level of 0.25 mJy/b at 235 MHz; Giacintucci et al. 2009b). This suggests that these cavities are no longer powered by the central AGN and are primarily driven by buoyancy. The isotropic distribution of the small, buoyantly driven cavities may be due to group "weather" as in the simulations of Bruggen et al. (2005) and Heinz et al. (2006). The origin of the group weather could be due to previous AGN outbursts or the sloshing of NGC 5044 with respect to the center of the group potential.

The enthalpy in a cavity is given by $H = \gamma PV/(\gamma - 1)$ and varies between 2.5 PV and 4 PV for $\gamma = 5/3$ and $\gamma = 4/3$. There are many uncertainties in estimating the ages of a cavities and McNamara & Nulsen (2007) list three possible methods for computing their ages, including: the sound crossing time, the buoyancy time and the refill time. We computed the three different age estimates for each cavity and found that the age estimates agree to within 30%. As a reasonable approximation, we compute the cavity power as $P_c = 4PV/t_s$, where t_s is the sound crossing time between the AGN and the center of the cavity. This gives a total cavity power for the three small radio quiet cavities (i.e., the SW, NW and NE cavities) of 9.2×10^{41} erg s^{-1} . The cavity power of the larger southern cavity is 5.6×10^{42} erg s^{-1} . For comparison, the bolometric luminosity of the hot gas within the central 10, 20 and 30 kpc is 2.1×10^{42} erg s^{-1} , 4.7×10^{42} erg s^{-1} and 7.1×10^{42} erg s^{-1} , respectively. This shows that the cavity power of the three smaller cavities, currently located between 4 and 7 kpc from the center

of NGC 5044, can balance about one-half of the radiative losses within the central 10 kpc. However, the combined cavity power of the three small cavities plus the larger southern cavity is sufficient to balance all radiative losses within the central 25 kpc. As discussed below, the presence of $H\alpha$ emitting gas within the central 5 kpc shows that as least some of the hot gas is able to cool to low temperatures.

Studies have shown that the mechanical cavity power far exceeds the radio luminosity of the X-ray cavities in groups and clusters of galaxies and that the ratio of cavity power to radio luminosity increases with decreasing radio luminosity (Birzan et al. 2004; 2008). In this paper we concentrate on the properties of the radio lobe toward the south-east observed at 610 MHz. The analysis of the extended radio emission at 235 MHz within the southern cavity is more complicated due to the larger beam size at 235 MHz ($22''$ by $16''$) and the $20''$ separation between the southern X-ray cavity and the central AGN. The GMRT data at 235 MHz will be discussed in more detail in Giacintucci et al. 2009b).

The monochromatic 610 MHz luminosity of the south-east radio lobe in NGC 5044 is $L_{610} = 9.3 \times 10^{36}$ erg s $^{-1}$ (Giacintucci et al. 2009a). Assuming a spectral index of $\alpha = 1$ and integrating between 10 MHz and 5 GHz (as in Birzan et al. 2004) gives a radio luminosity of $L_R = 5.7 \times 10^{37}$ erg s $^{-1}$, which is a factor of approximately 100 less than the least luminous radio filled cavity studied in the Birzan et al. (2004) sample. The ratio of cavity power to radio luminosity, assuming the cavity is the same size as the radio lobe, is $P_c/L_R = 1.3 \times 10^3$ for the south-east radio lobe in NGC 5044. Using the relation between cavity power and radio luminosity (eq. 12 in Birzan et al. 2008) along with the observed radio luminosity of the south-east radio lobe, gives a predicted cavity power of $P_c = 4.0 \times 10^{41}$, which is only 40% less than the observed value. While this is only one extra data point, it shows that there is some evidence that the relation between P_c and L_R derived in Birzan et al. (2008) extends over 8 orders of magnitude in L_R .

We showed above that we cannot place very tight constraints on the amount of hot thermal gas within the cavities in NGC 5044 due to the hard X-ray emission from unresolved LMXBs. Constraints on the particle content within the radio lobes observed in groups and clusters can be obtained by assuming the lobes are in pressure equilibrium with the ambient gas (Dunn & Fabian 2004; Birzan et al. 2008; Croston et al. 2008). The total particle energy within a radio lobe can be written as $E_p = kE_e$, where E_e is the energy in relativistic electrons emitting synchrotron radiation at frequencies greater than 10 MHz. Using the observed 610 MHz radio luminosity from the south-east radio lobe along with the expression for E_e in Pacholczyk (1970), assuming $\alpha = 1$, gives:

$$E_p = 6.0 \times 10^{54} \left(\frac{B}{1 \mu G} \right) k \text{ erg}$$

The energy in the magnetic field is $E_B = B^2 \phi V / (8\pi)$, where V is the volume of the radio lobe and ϕ is the volume filling factor. For the south-east radio lobe, this gives:

$$E_B = 1.4 \times 10^{54} \left(\frac{B}{1 \mu G} \right)^2 \phi \text{ erg}$$

Assuming energy equipartition then gives:

$$B_{eq} = 1.5 \left(\frac{k}{\phi} \right) \mu G$$

Combining the assumptions of energy equipartition and pressure equilibrium between the ambient medium and the radio lobe ($P_T = kE_e / (3V\phi) + E_B / (V\phi)$) gives $k/\phi = 1.2 \times 10^4$ and $B_{eq} = 23 \mu G$.

Performing a similar analysis, Dunn & Fabian (2004) and Birzan et al. (2008) obtained values of k/ϕ up to approximately 4000 based on samples of radio lobes in mostly rich clusters of galaxies. This comparison shows that the non-radiating energy content of the south-east radio lobe in NGC 5044 is significantly greater than that in the larger radio lobes analyzed in these two samples. Birzan et al. (2008) found a correlation between k/ϕ and the synchrotron age of the radio lobe. Based on an analysis of radio lobes in a sample of groups of galaxies, Croston et al. (2008) noted that "plumed" radio lobes were more under-pressurized than radio lobes connected with a jet. Both of these results suggests that k/ϕ increases with time after the radio lobes are no longer powered by the central AGN. The most likely origins for this increase in k/ϕ are the entrainment of thermal gas and aging of the relativistic electron population. While we cannot estimate the synchrotron age for the south-east radio lobe without knowing the break frequency in the radio spectrum, the sound crossing time between the AGN and the south-east lobe is only 2×10^7 yr, so it must be fairly young. However, the torus-like structure of the south-east radio lobe and the fact that a cool filament of gas is currently threading the torus suggest that it may have already entrained a significant amount of ambient gas.

8.2. Comparison with Optical and IR observations

Most of the $H\alpha$ emission from NGC 5044 is contained in a broad filament aligned in a north to south direction (Macchetto et al. 1996). The northern portion of the $H\alpha$ filament has an extent of approximately 7 kpc and lies along the eastern rim of the NW cavity. The southern portion of the filament trails the southern cavity, but unfortunately, a "ghost image mutilated the $H\alpha$ + [NII] emission map" beyond approximately 5 kpc, which is only half of the distance to the center of the south-east radio torus. Temi et al. (2007) showed that there is some evidence for distributed PAH emission with the same morphology as the southern extension of the $H\alpha$ filament from the *Spitzer* observation of NGC 5044. Spatial correlations between the $H\alpha$ emission, PAH emission and X-ray morphology were also noted by Gastaldello et al. (2008) based on the earlier 20 ksec Chandra observation.

Caon et al. (2000) obtained long-slit spectroscopy at three position angles across the $H\alpha$ filament. The gas in the northern extension of the filament is mostly red-shifted with respect to NGC 5044 with a peak velocity of approximately 100 km s^{-1} . The kinematics of the gas in the southern extension of the $H\alpha$ filament are more chaotic with red and blue shifted velocities between $\pm 100 \text{ km s}^{-1}$. Without knowing the inclination of the $H\alpha$ filament relative to the plane of the sky, we cannot say which gas is in-falling and which gas is outflowing. However, the kinematics of the gas in the $H\alpha$ filament are very similar to the kinematics of the $H\alpha$ filaments in NGC 1275 observed by Hatch et al. (2006) and are probably due to dredge up and subsequent infall behind the buoyantly rising cavities. Temi et al. (2007) also argued that the extended dust distribution, as highlighted by the PAH emission, could be due to the break up of a central dusty disk followed by buoyant uplifting behind the southern X-ray cavity.

The kinematics of the warm 10^4 K gas are inconsistent with

TABLE 4
PREDICTED COUNT RATES FOR ENTRAINED THERMAL GAS IN THE CAVITIES

| kT (keV) | n_e (cm^{-3}) | R(5.0-7.0 keV) ct s $^{-1}$ |
|-------------|-------------------------------|--------------------------------|
| 2.0 | 8.0×10^{-3} | 1.61×10^{-5} |
| 3.0 | 5.3×10^{-3} | 1.31×10^{-5} |
| 4.0 | 4.0×10^{-3} | 9.97×10^{-6} |
| 5.0 | 3.2×10^{-3} | 7.68×10^{-6} |
| 10.0 | 1.6×10^{-3} | 2.45×10^{-6} |

Notes: This table gives the predicted 5-7 keV count rate for thermal gas in pressure equilibrium within the 4 cavities assuming gas temperatures between 2 and 10 keV. The electron number density, n_e , is derived by assuming pressure equilibrium. The 3σ upper limit on the observed 5-7 keV count rate within these cavities is 1.1×10^{-4} ct s $^{-1}$.

an external origin for the gas (Caon et al. 2000), so the gas could arise from either stellar mass loss or radiative cooling of the hot ambient gas. The total mass of H α emitting gas is $8.5 \times 10^5 M_\odot$ (Macchetto et al. 1996). From the H α image, it appears that most of the warm gas originates from within the central 2 kpc, and is then dredged outward. Fitting a de Vaucouleurs profile to the 2MASS K-band image of NGC 5044 gives a deprojected K-band luminosity within the central 2 kpc of $L_K = 6.5 \times 10^9 L_\odot$ (David et al. 2009). Using the stellar mass loss rate in Athey et al. (2002) gives $\dot{M}_* = 0.012 M_\odot \text{ yr}^{-1}$ within this region. The cooling time of the hot gas within the central 2 kpc is 4.1×10^7 yr and the mass cooling rate is approximately $\dot{M}_h = 0.9 M_\odot \text{ yr}^{-1}$. Thus, even if only 2% of the hot gas is able to cool to low temperatures, radiative cooling of the hot gas would still be the dominant mass supply mechanism for the warm gas in NGC 5044.

8.3. Residual Motion of NGC 5044

NGC 5044 has two semi-circular cold fronts at projected distances of 30 and 50 kpc from the center of the group. Cold fronts are commonly found near the central dominant galaxy in clusters and may be due to merger induced sloshing (Ascasibar & Markevitch 2006; Markevitch & Vikhlinin 2007). Based on an optical study of the galaxies in the NGC 5044 group, Cellone & Buzzoni (2005) found that NGC 5044 has a peculiar velocity of approximately 140 km s^{-1} with respect to the velocity centroid of the other galaxies in the group. One possible candidate for perturbing NGC 5044 is a sub-group of galaxies toward the NE identified by Mendel et al. (2008), but this group lies at a projected distance of 1.5 Mpc. Another possible candidate is the optically perturbed spiral galaxy NGC 5054 which is located at a projected distance of 300 kpc toward the southeast, has a blue-shifted velocity of 960 km s^{-1} and is only two magnitudes fainter than NGC 5044.

Single spiral features have been observed in the X-ray images of the Ophiuchus cluster (Sanders and Fabian 2002), the Perseus cluster (Churazov et al. 2000; Fabian et al. 2006) and A2029 (Clarke et al. 2004). Ascasibar & Markevitch (2006) have shown through numerical simulations that single spiral arms of cool gas are commonly produced by sloshing of the

central galaxy, however, none of their simulations produce two spiral arms like those observed in NGC 5044. The spiral arms in NGC 5044 are more similar to the spiral arms (or "hour glass" shaped feature) in NGC 4636 (Jones et al. 2002; Baldi et al. 2009). X-ray spectral analysis of the gas in the spiral arms in NGC 4636 shows that this gas was recently shocked, probably during the inflation of the radio emitting plasma currently observed between the spiral arms (Jones et al. 2002; Baldi et al. 2009). The spiral arms in NGC 5044 are cooler than the surrounding gas. Also, no radio emission is detected at either 235 MHz or 610 MHz interior to the spiral arms like that observed in NGC 4636. Thus, if the spiral arms in NGC 5044 were created by the inflation of radio bubbles, this must have occurred during an earlier radio outburst. This would also give the gas in the spiral arms time to cool by adiabatic expansion if they were initially shocked.

9. SUMMARY

The Chandra observation of NGC 5044 provides us with some insights on the AGN-cooling flow feedback mechanism that cannot be attained from observing more distant rich clusters. Unlike the large, energetic and nearly bi-polar distribution of the X-ray cavities observed in many rich clusters, the inner 5-10 kpc of NGC 5044 is filled with many small radio quiet cavities. Since these small cavities are probably no longer momentum driven by the central AGN, their motion will be driven by the group weather as they buoyantly rise outward. Hence, most of their energy will be deposited within the group center and isotropized by the group weather. Such a situation could be a common feature in the center of groups and clusters, in which most of the central cooling and star formation is suppressed by many small, weather driven bubbles, while the less frequent larger outbursts predominately heat the gas at larger radii and supply some of the "pre-heating" required to break the self-similarity of groups and clusters.

We would like to thank T. Venturi and R. Athreya for help with the GMRT observations and M. Markevitch with information about the ACIS background. This work was supported in part by NASA grant GO7-8127X.

REFERENCES

- Ascasibar, Y., Markevitch, M. 2006, 650, 102.
Athey, A., Bregman, J., Bregman, J., Temi, P. & Sauvage, M. 2002, ApJ, 571, 272.
Baldi, A. et al. 2009 (in preparation).
Birzan, L., Rafferty, D., McNamara, B., Wise, M. & Nulsen, P. 2004, ApJ, 607, 800.
Birzan, L., McNamara, B., Nulsen, P., Carilli, C. & Wise, M. 2008, ApJ, 686, 859.

- Blanton, E., Sarazin, C. & McNamara 2003, ApJ, 585, 227.
 Brassington, N. et al. 2008, ApJSuppl, 179, 142.
 Bruggen, M., Ruszkowski, M. & Hallman, E. 2005, ApJ, 630, 740.
 Buote, D. 1999, MNRAS, 309, 685.
 Buote, D., Lewis, A., Brighenti, F. & Mathews, W. 2003, 594, 741.
 Caon, N., Macchetto, D. & Pastoriza, M. 2000, ApJSuppl, 127, 39.
 Cellone, S. & Buzzoni, A. 2005, MNRAS, 356, 41.
 Churazov, E., Bruggen, M., Kaiser, C., Bohringer, H. & Forman, W. 2001, ApJ, 554, 261.
 Churazov, E., Forman, W., Jones, C. & Bohringer, H. 2000, A&A, 356, 788.
 Clarke, T., Blanton, E. & Sarazin, C. 2004, ApJ, 616, 178.
 Croston, J., Hardcastle, M., Birkinshaw, M., Worrall, D. & Laing, R. 2008, MNRAS, 386, 1709.
 Croton, D. et al. 2006, MNRAS, 365, 11.
 David, L., Jones, C., Forman, W. & Daines, S. 1995, ApJ, 428, 544.
 David, L., Nulsen, P., McNamara, B., Forman, W., Jones, C., Ponman, T., Robertson, B., Wise, M. 2001, ApJ, 557, 546.
 David, L., Jones, C., Forman, W., Murray, S. 2005, ApJ, 635, 1053.
 David, L., Jones, C., Forman, W., Vargas, I. M., Nulsen, P. 2006, ApJ, 653, 207.
 David, L. et al. 2009 (in preparation).
 Di Matteo, T., Allen, S., Fabian, A. Wilson, A. & Young, A. 2003, ApJ, 582, 133.
 Dunn, R. & Fabian, A. 2004, MNRAS, 355, 862.
 Fabian, A., Sanders, J., Allen, S., Crawford, C., Iwasawa, K., Johnstone, R., Schmidt, W. & Taylor G. 2003, MNRAS, 344, 43.
 Fabian, A., Sanders, J., Taylor, G. & Allen, S. 2005, MNRAS, 360, 20.
 Fabian, A., Sanders, J., Taylor, G., Allen, S., Crawford, C., Johnstone, R. & Iwasawa, K. 2006, MNRAS, 366, 417.
 Finoguenov, A., Ponman, T., Osmond, J. & Zimer, M. 2007, MNRAS, 374, 737.
 Forman, W. et al. 2007, ApJ, 665, 1057.
 Gardini, A. 2007, A&A, 464, 143.
 Gastaldello, F., Buote, D., Temi, P., Brighenti, F., Mathews, W. & Ettori, S. 2008 (astro-ph 0807.3526).
 Gebhardt, K. et al. 2000, ApJ, 539, L13.
 Giacintucci, S. et al. 2009 (in preparation).
 Greesse, N. & Sauval, A. 1998, Sp. Sci. Rev., 85, 161.
 Hatch, N., Crawford, C., Johnstone, R., Fabian, A. 2006, MNRAS, 367, 433.
 Heinz, S., Bruggen, M., Young, A. & Levesque, E. 2006, ApJ, 373, L65.
 Jones, C., Forman, W., Vikhlinin, A., Markevitch, M., David, L., Warmflash, A., Murray, S. & Nulsen, P. 2002, ApJ, 567, L115.
 Kim, D. & Fabbiano, G. 2004, ApJ, 611, 846.
 Kraft, R., Kregenow, J., Forman, W., Jones, C., Murray, S. 2001, ApJ, 560, 675.
 Loewenstein, M., Mushotzky, R., Angelini, L., Arnaud, K. & Quataert, E. 2001, ApJ, 555, L21.
 Macchetto, F., Pastoriza, M., Caon, N., Sparks, W., Giavalisco, M., Bender, R., Capaccioli, M. 1996, A&A Suppl., 120, 463.
 Markevitch, M. & Vikhlinin, A. 2007, Phys. Rep., 443, 1.
 Markevitch, M. 2008 (private communication).
 McNamara, B. et al. 2000, ApJ, 534, 135.
 McNamara, B. & Nulsen, P. 2007, ARA&A, 45, 117.
 Mendel, J., Proctor, R., Forbes, D. & Brough, S. 2008, MNRAS, 389, 749.
 Moretti, A., Campana, S., Lazzati, D. & Tagliaferri, G. 2003, ApJ, 588, 696.
 Nulsen, P., McNamara, B., Wise, M. & David, L. 2005, ApJ, 628, 629.
 O'Sullivan, E. et al. 2009 (in preparation).
 O'Sullivan, E., Vrtilik, J. & Kempner, J. 2005, ApJ, 624, L77.
 Pacholczyk, A. 1970, in Radio Astrophysics (ed. W. Freeman and Company).
 Peterson, J., Kahn, S., Paerels, F., Kaastra, J., Tamura, T., Bleeker, J., Ferrigno, C. & Jernigan, J. 2003, ApJ, 590, 207.
 Peterson, J. & Fabian, A. 2006, Phys Rep., 427, 1.
 Revaz, Y., Combes, F. & Salome, P. 2008, A&A, 477, L33.
 Sanders, J. & Fabian, A. 2002, MNRAS, 331, 273.
 Sarazin, C., Irwin, J. & Bregman, J. 2001, ApJ, 556, 533.
 Sparks, W., Disney, M., Wall, J. & Rodgers, A. 1984, MNRAS, 207, 445.
 Tamura, T., Kaastra, J., Makishima, K. & Takahashi, I. 2003, A&A, 399, 497.
 Temi, P., Brighenti, F. & Mathews, W. 2007, ApJ, 666, 222.